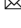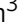## ARTICLE

Check for updates

Nano-patterning on multilayer MoS$_2$ via block copolymer lithography for highly sensitive and responsive phototransistors

Heekyeong Park[1,7], Jiyoul Lee[2,7], Gyuchull Han [3,7], AbdulAziz AlMutairi[3,7], Young-Hoon Kim[4], Jaichan Lee[1], Young-Min Kim[4,5✉], Young Jun Kim[6✉], Youngki Yoon[3✉] & Sunkook Kim [1✉]

Indirect bandgap of multilayer molybdenum disulfide has been recognized as a major hindrance to high responsivity of MoS$_2$ phototransistors. Here, to overcome this fundamental limitation, we propose a structural engineering of MoS$_2$ via nano-patterning using block copolymer lithography. The fabricated nanoporous MoS$_2$, consisting of periodic hexagonal arrays of hexagon nanoholes, includes abundant edges having a zigzag configuration of atomic columns with molybdenum and sulfur atoms. These exposed zigzag edges are responsible for multiple trap states in the bandgap region, as confirmed by photo-excited charge-collection spectroscopy measurements on multilayer nanoporous MoS$_2$ phototransistors, showing that in-gap states only near the valence band can result in a photogating effect. The effect of nano-patterning is therefore to significantly enhance the responsivity of multilayer nanoporous MoS$_2$ phototransistors, exhibiting an ultra-high photoresponsivity of 622.2 A W^{-1}. Our nano-patterning of MoS$_2$ for photosensing application paves a route to structural engineering of two-dimensional materials for highly sensitive and responsive optoelectronic devices.

[1] Department of Advanced Materials and Science Engineering, Sungkyunkwan University (SKKU), Suwon, Republic of Korea. [2] Department of Nanotechnology Engineering & Department of Smart Green Technology Engineering, Pukyong National University, Busan, Republic of Korea. [3] Waterloo Institute for Nanotechnology (WIN) & Department of Electrical and Computer Engineering, University of Waterloo, Waterloo, ON, Canada. [4] Department of Energy Science, Sungkyunkwan University (SKKU), Suwon, Republic of Korea. [5] Center for Integrated Nanostructure Physics, Institute for Basic Science (IBS), Suwon, Republic of Korea. [6] BioNano Health Guard Research Center (H-GUARD), Daejeon, Republic of Korea. [7] These authors contributed equally: Heekyeong Park, Jiyoul Lee, Gyuchull Han, AbdulAziz AlMutairi. ✉email: mirage91@naver.com; junkim@kribb.re.kr; ykyoon@uwaterloo.ca; intel0616@gmail.com

Due to the dramatic advance in complementary metal-oxide-semiconductor (CMOS) image sensors in the past decades, they are widely used in present-day smartphones and digital cameras[1,2]. However, one of the most critical bottlenecks of CMOS image sensors is the size that is smaller than target objects, making one-to-one direct mapping between a sensor and an object impossible without using lenses. This leads to the limitation of their use for touch-based applications such as interactive display, fingerprint security, and human-robot interaction. In this regard, thin-film phototransistor-based image sensors can be a talented alternative as they can be easily scaled up with lower process costs, provide new functionality such as flexibility, and extend the boundaries of practical applications[3–5]. Therefore, exploring channel materials of thin-film transistors (TFTs) that can bring high carrier mobility, high photoresponsivity, and mechanical flexibility is of great importance to make a new breakthrough for next-generation optoelectronic devices[6–8].

Two-dimensional (2D) layered nanomaterials, such as transition metal dichalcogenides (TMDs), can be promising contenders for the active material of thin-film phototransistor image sensors[9–12] due to their excellent optical and electrical performances as well as mechanical stability[13–15]. The optical characteristics of TMDs significantly vary with the thickness of the material[13,16,17]. In general, direct bandgap monolayer TMDs exhibit high photoresponsivity, whereas multilayer TMDs show relatively low photoresponsivity due to their indirect bandgap[8,18]. However, multilayer TMDs have been recognized as being more suitable for versatile photodetector applications than monolayer TMDs, with great benefits arising from the higher carrier density[19] and the wider spectral response from near-infrared to ultraviolet (UV)[18], as well as easier fabrication.

Recently, structural engineering of TMDs has drawn significant attention as it can alter the fundamental material properties[20]. Several approaches to overcome the limitation of the low photoresponsivity of multilayer TMDs have been reported, which include stacking of heterostructures[21], decoration with quantum dots[22,23], and introduction of different alignment directions[24]. On the other hand, nano-patterning, a relatively new technique for structural engineering, can provide a novel route to tune the optical and electrical performances of 2D materials by directly modifying the electronic states. For example, graphene, which has a significant limitation for electronic applications due to its zero bandgap, can obtain a finite bandgap through a nanoporous patterning by inducing quantum confinement effect[25–28]. In addition, Kim et al.[29] reported that nanopore-patterned multilayer molybdenum disulfide (MoS$_2$) presents a large photoluminescence emission peak similar to the direct bandgap monolayer MoS$_2$. However, experimental work has not been reported for the nanoporous MoS$_2$ device and its optoelectronic characteristics.

Here, we present the nano-patterning of multilayer MoS$_2$ to achieve high-performance multilayer MoS$_2$ phototransistors. The block copolymer (BCP), which consists of two homopolymers and forms periodic nanostructures through phase separation[30–32], was used to pattern multilayer MoS$_2$ into a nanoporous structure containing an array of periodic nanoholes. It should be noted that the photoresponsivity of our nanoporous MoS$_2$ phototransistors (622.2 A W^{-1}) is even higher than the direct bandgap monolayer MoS$_2$ counterparts reported in the literature under similar optical power densities and wavelengths of incident light[33–35]. To investigate a fundamental origin of this ultra-high responsivity from the nanoporous MoS$_2$ phototransistors, we explored the exposed edge structure of the nanoporous MoS$_2$ by Raman spectroscopy, X-ray photoelectron spectroscopy (XPS), and scanning transmission electron microscopy (STEM). Photo-excited charge-collection spectroscopy (PECCS) measurement[36] was performed to develop

understanding of the newly generated trap states in the bandgap by adopting the nanohole structure on MoS$_2$. Finally, device simulation elucidated the mechanism of photoresponse in nanoporous MoS$_2$ phototransistors.

Results

Nano-scale patterning on multilayer MoS$_2$. A nano-scale template based on the phase separation behavior of the BCP was utilized to fabricate the nanoporous structure on multilayer MoS$_2$ films. Figure 1a shows the fabrication processes to achieve nanoporous MoS$_2$. MoS$_2$ multilayer sheets were separated from bulk MoS$_2$ by a mechanical exfoliation and then located onto a Si/SiO$_2$ substrate. SiO$_2$ with a thickness of 10 nm was deposited on the MoS$_2$ surface by an electron-beam (e-beam) evaporator to lead to covalent bonds with the grafting layer of a random copolymer (RCP) as well as to prevent damage to MoS$_2$ during the etching process[26,31,37]. The BCP was spin-coated on the RCP film and annealed at 230 °C to produce cylindrical phase separation of polymethyl methacrylate (PMMA) and polystyrene (PS). The cylindrical PMMA phase was selectively removed by shining UV light on the BCP film and acetic acid, resulting in the nanoporous template of PS. A field emission-scanning electron microscopy (FE-SEM) image of the template shows a uniform and periodic structure of circular nanoholes with an average diameter of 21.1 ± 1.1 nm (Supplementary Fig. 1). Moreover, the nanohole dimension could be controlled from 24.7 to 30.8 nm by simply changing the treatment time of oxygen (O$_2$) plasma reactive-ion etching (RIE), as confirmed by FE-SEM images (Supplementary Fig. 2a–d) and the linear relationship between the hole diameter and the treatment time (Supplementary Fig. 2e). Using the BCP as a template, the underlying SiO$_2$ was perforated by sulfur hexafluoride (SF$_6$) plasma RIE. Finally, uniform hexagon nanoholes were formed on the multilayer MoS$_2$ sheets through two consecutive steps: (i) dry etching using boron trichloride (BCl$_3$) plasma RIE and (ii) wet etching using potassium ferricyanide solution. After removing the remaining SiO$_2$ layer, the patterned surface of MoS$_2$ was observed by annular dark field (ADF)-STEM, as shown in Fig. 1b. The uniformity of the nanoholes was validated by calculating the hole diameters in a large-area ADF-STEM image (Supplementary Fig. 3a), in which the average hole diameter was turned out to be 26.2 ± 2.3 nm (Supplementary Fig. 3b). The substructure of the hole distribution was consistently characterized. The hexagonal nanoholes with an incircle radius (r_h) of ~12 nm were mostly distributed into hexagonal array with a secondary incircle radius (R_{h-h}) of ~40 nm (Fig. 1b). This crystallographic feature of the nanoporous MoS$_2$ film was corroborated by the fast Fourier transform (FFT) pattern analysis of the ADF-STEM image (Supplementary Fig. 3a), which is equivalent to electron diffraction of the corresponding region (Fig. 1c). The first diffraction ring shows the overall periodicity of the nanoholes, with a length repetition of ~40 nm, and the outmost faint diffraction ring shows the hexagonal shape of the nanoholes, with r_h of ~12 nm. The spotty diffraction pattern indicates that the nanoporous MoS$_2$ has a multi-domain hexagonal array of the hexagonal nanoholes. The ADF intensity profile across several hexagonal nanoholes (Supplementary Fig. 3c) supports this 2D length repetition in the nanoporous MoS$_2$. According to STEM-energy dispersive X-ray spectroscopy (EDX) elemental mapping of Mo K, S K, and Si K peaks on the nanoporous MoS$_2$ transferred to a copper grid (Fig. 1d), it is clarified that the chemical composition of the nanoporous structure is MoS$_2$. The thickness of the nanoporous MoS$_2$ nanosheet was estimated to be ~7.6 nm based on the cross-section ADF-STEM image (the bottom of Fig. 1d), which corresponds to 11 layers of MoS$_2$.
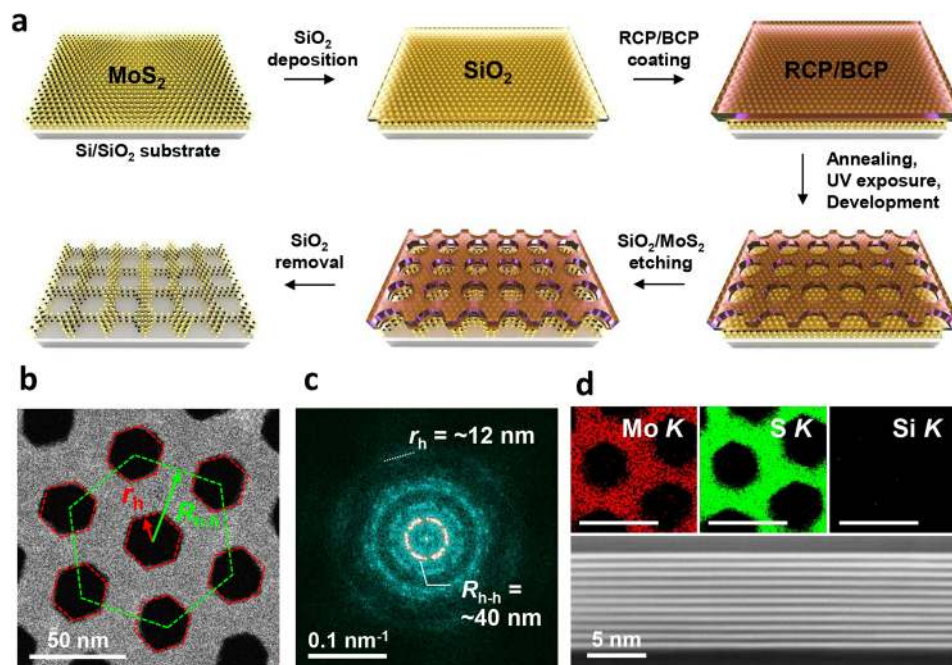
Fig. 1 Preparation and microscopic characterization of the nano-patterned MoS$_2$ multilayer. a A schematic illustration of nano-scale patterning process on multilayer MoS$_2$. **b** ADF-STEM image showing an array of nanoholes in the multilayer MoS$_2$. **c** FFT pattern representing a crystallographic hexagonal array of hexagon holes (from Supplementary Fig. 3a). **d** STEM-EDX elemental mapping (top panels) for Mo K, S K, and Si K peaks (scale bars of 50 nm) and cross-sectional view (bottom panel) of the multilayer nanoporous MoS$_2$.

Hexagonal nanohole edges in nanoporous MoS$_2$. In order to confirm the material characteristics of the multilayer nanoporous MoS$_2$ regarding the formation of nanoholes, Raman spectroscopy, and XPS were employed. In Fig. 2a, a characteristic Raman doublet of pristine MoS$_2$ is present at 383.7 cm^{-1} for E^1_{2g} (in-plane mode) and 407.5 cm^{-1} for A_{1g} (out-of-plane mode), which corresponds to multilayer MoS$_2$[38]. The peak positions were rarely changed in the nanoporous MoS$_2$, whereas the relative intensity of E^1_{2g}/A_{1g} was reduced from 0.824 for pristine MoS$_2$ to 0.604 for nanoporous MoS$_2$. This noticeable change is in good agreement with the increased number of edges in nanoporous MoS$_2$ because A_{1g} is preferentially excited for edge-terminated films compared to E^1_{2g} due to their polarization dependence[20,29,39,40]. A decrease in the peak intensity of E^1_{2g}/A_{1g} was consistently observed for nine different nanoporous MoS$_2$ films (inset of Fig. 2a), strongly supporting the reliability of the manufacturing process.

Figure 2b shows XPS spectra of Mo 3d and S 2p core levels of pristine MoS$_2$ and nanoporous MoS$_2$. To compensate for sample charging, all the XPS spectra were calibrated by C 1s peak located at 284.5 eV. Most intense doublets of the Mo 3d and S 2p were observed at 229.15 eV (Mo^{4+} 3$d_{5/2}$) and 161.96 eV (S^{2-} 2$p_{3/2}$), respectively, in both pristine and nanoporous MoS$_2$. However, these two doublets in the nanoporous MoS$_2$ had wider full-width at half-maximum (FWHM) than pristine MoS$_2$. Therefore, we deconvoluted the Mo 3d peak into three component peaks corresponding to intrinsic MoS$_2$ (i-MoS$_2$), substoichiometric MoS$_2$ (s-MoS$_2$), and molybdenum oxide (MoO$_3$) bonding[41–44]. The peak of s-MoS$_2$ is attributed to the electronic structure different from stoichiometric MoS$_2$ (ratio of S/Mo = 2) because there are fewer S atoms around Mo atoms at exposed edge sites[44]. The doublet of s-MoS$_2$ at 228.55 eV (Mo^{4+} 3$d_{5/2}$) and 231.68 eV (Mo^{4+} 3$d_{3/2}$), respectively, was observed in both the pristine and the nanoporous MoS$_2$, whereas the atomic ratio of s-MoS$_2$ increased from 6.32% in pristine MoS$_2$ to 14.41% in nanoporous MoS$_2$ (Supplementary Table 1). In addition, as evidenced by a decrease of the ratio of S^{2-} 2p to Mo^{4+} 3d (i-MoS$_2$ + s-MoS$_2$)

from 2.00 to 1.89 after nanoporous patterning, the degree of the edge exposure introduced by formation of nanoholes on multilayer MoS$_2$ can be quantitatively estimated.

The MoO$_3$ may be derived from oxidation of surface and etched region of MoS$_2$ when exposed to air. An atomic ratio of Mo^{6+} 3d (MoO$_3$), located at 232.16 eV (Mo $^{6+}$ 3$d_{5/2}$) and 235.29 eV (Mo^{6+} 3$d_{3/2}$), rarely increased from the pristine (10.90%) to the nanoporous MoS$_2$ (12.11%) due to the protective effect of the SiO$_2$ layer on the MoS$_2$ film. In addition, the absence of Cl 2p, B 1s, N 1s peaks (Supplementary Fig. 4a–c) verifies the protective function of the SiO$_2$ layer, which helps to prevent chemical contaminations during the dry etching with BCl$_3$ plasma RIE and wet etching with potassium ferricyanide solution.

To determine the atomic configuration of the hexagonal nanohole edges in the nanoporous MoS$_2$, the atomic structures of multilayer MoS$_2$ showing a stacking sequence as well as the edge of the nanohole should be scrutinized. Figure 2c presents a typical hexagonal shape of the nanohole in the nanoporous MoS$_2$. The inset in Fig. 2c shows the selected area diffraction pattern (SADP) for the MoS$_2$ multilayer region, suggesting a 2H-MoS$_2$ structure (S.G. = $P6_3/mmc$) with an AA′ stacking configuration in which atomic columns along the [001] orientation are mixed with Mo and S atoms. To identify the edge structure of the hexagonal hole, atomic-scale ADF-STEM observation of sides and apexes of the hexagonal hole was performed, as shown in Fig. 2d–h. According to atomic configuration of the top MoS$_2$ layer inserted in each figure, the nanohole edges mostly have a zigzag configuration of atomic columns except for a few local disordered regions.

It is worth noting that the nanohole shape was modified when further etching was carried out on the nanohole. The nanohole structure was circular when the MoS$_2$ was dry etched with BCl$_3$ plasma RIE (Supplementary Fig. 5a). When the MoS$_2$ was dipped in potassium ferricyanide solution, the circular-shaped nanoholes became hexagonal structure (Supplementary Fig. 5b, c). The wet etching process changed not only the shape of the holes, but also the atomic configuration of nanohole edges. While MoS$_2$ has two
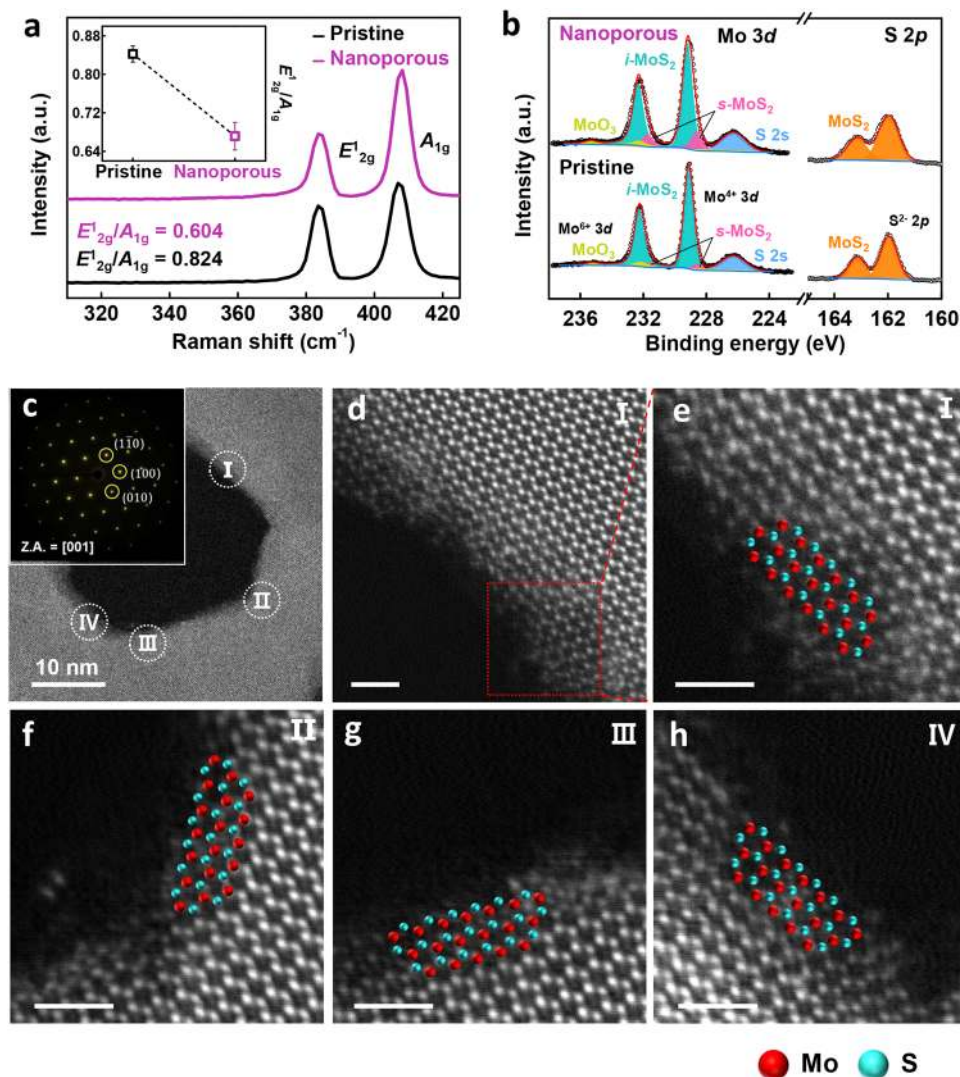
Fig. 2 Edge structure of the hexagonal nanohole in the multilayer nanoporous MoS₂. a Raman and **b** XPS spectra of multilayer pristine and nanoporous MoS₂, respectively. **c**, ADF-STEM image of a typical hexagonal nanohole in the nanoporous MoS₂ (inset is SADP exhibiting a typical 2H-MoS₂ structure). **d–h** Atomic-scale ADF-STEM observations of the four regions denoted by I, II, III, and IV in **c** (scale bars of 1 nm).

different edge types of zigzag and armchair[45,46], the zigzag configuration was found more dominant in the hexagonal nanoholes. Such transformation of edge configuration can be assigned to the higher thermodynamic stability of the zigzag configuration in comparison to that of the armchair configuration[47,48]. It can be reasoned that the energetically less favorable armchair structure gradually changed to more favorable zigzag structure. An in-depth study of the dependence of the hole shape on the crystallographic orientation and surface energy of MoS₂ is still in progress, which is beyond the scope of this study. Given the AA′ stacking configuration of the MoS₂ sample, the exposed atomic terminations at every edge are regarded as a mixture of Mo- and S-terminated zigzag structures layer by layer, which can be confirmed by the same intensity profiles of Mo K and S K peaks extracted from edge to edge across the hole (Supplementary Fig. 6c) in the STEM-EDX elemental mapping data (Supplementary Fig. 6a, b).

Electronic structural characterization of nano-patterned MoS₂. As opposed to a pristine MoS₂, it is expected that the nanoporous MoS₂ has a different band structure due to the abundant broken

bonds in the MoS₂ lattice represented by the exposure of zigzag edges. In order to explore the electric states of the nanoporous MoS₂, PECCS measurement was conducted. The PECCS is a useful tool to probe the sub-states inside the bandgap by calculating a photoinduced threshold voltage shift (ΔV_{TH}) from phototransistors[36]. Figure 3a, b show photo-excited transfer curves of the multilayer nanoporous MoS₂ TFTs under monochromatic light illumination with various wavelengths and photon energy dependence of ΔV_{TH} extracted from individual photoexcited transfer curves. In Fig. 3b, it was observed that ΔV_{TH} values of both multilayer devices, the pristine and nanoporous MoS₂ TFTs, gradually decreased as the photon energy of the illuminated monochromatic light increased up to the edge of the bandgap energy, and then increased rapidly above the bandgap energy. However, compared to the pristine MoS₂ TFT, it can be seen that the V_{TH} of the nanoporous MoS₂ TFT shifted significantly, implying remarkable interband charge transitions[49]. The areal density of states (DOS) of the multilayer MoS₂ TFTs can be extracted by distinguishing the excited charge values from the incident photon energy from the ΔV_{TH} dependent curves. Figure 3c presents the experimentally obtained spectral DOS of both multilayer pristine MoS₂ and nanoporous MoS₂ TFTs. They
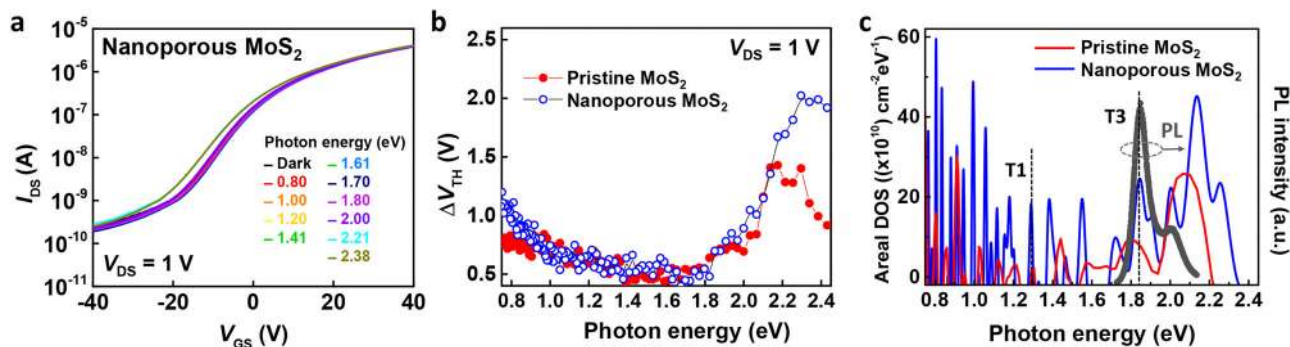
Fig. 3 Optoelectronic characteristics of MoS2 TFTs. a Photo-excited transfer characteristics of the multilayer nanoporous MoS_2 TFT under monochromatic light illumination with various wavelengths. **b** Dependence of ΔV_{TH} on the incident photon energy, which was extracted from individual photo-excited transfer curves of the MoS_2 TFTs. **c** Photon energy-dependent areal DOS profiles of the multilayer pristine and nanoporous MoS_2 TFTs. The photoluminescence (PL) spectra (bold gray line) of the nanoporous MoS_2 is overlaid on the graph to compare the peak position observed by PECCS and the interband transitions measured by PL.

show the charge transition peaks corresponding to the energy states assigned as T1 (~1.30 eV, indirect bandgap) and T3 (~1.85 eV, direct bandgap)[49] matched with the photoluminescence spectra of MoS_2. More importantly, additional peaks were observed in the photon energy region lower than the bandgap energy, which correspond to the interband charge transitions. In particular, the experimentally observed interband states in the nanoporous MoS_2 were overwhelmingly more than for the pristine MoS_2, which seems to have been caused by the abundant exposure of edge atoms in nanoporous structure. Here, note that the T3 transition peaks of the pristine and nanoporous MoS_2 were not perfectly matched at the same energy due to the thickness difference between the two MoS_2 flakes, rather than the formation of nanoporous structure.

Multilayer nanoporous MoS_2 phototransistors. In general, in-gap states can directly influence the optoelectronic properties of materials. It has been reported that the in-gap states induced by interstitial atoms in multilayer molybdenum diselenide (MoSe₂) TFTs can result in significant photogating effect and high photoresponsivity under illumination[49]. In this study, we explored the characteristics of the nanoporus MoS_2 phototransistors. Figure 4a shows a SEM image of a nanoporous MoS_2 TFT, in which source and drain electrodes were positioned on the nanoporous MoS_2 with a channel area of 34.28 μm². The transfer characteristics of the nanoporous MoS_2 TFT were measured under the illumination of different incident power densities (P_{inc}) with light wavelength (λ_{ex}) of 405 nm and a drain voltage (V_{DS}) of 1 V (Fig. 4b). The same measurement has been carried out for a pristine multilayer MoS_2 TFT with a channel area of 56.28 μm² (Fig. 4c) for comparison. Although a significant increase in OFF-state current under illumination was commonly observed in both devices (due to the conductivity increase by the photoinduced excess carriers; i.e., the photoconductive effect), only the nanoporous MoS_2 phototransistor showed a negative V_{TH} shift (i.e., the photogating effect). Consequently, the photocurrent (I_{ph} = $I_{illumination}$ − I_{dark}) of the nanoporous MoS_2 TFT presented a remarkable increase in the ON-state (i.e., at high gate voltages) (Supplementary Fig. 7a), unlike the pristine MoS_2 TFT (Supplementary Fig. 7b). We also extracted photoresponsivity ($R = I_{ph}/P_{inc}$) of both devices as a function of P_{inc} (Fig. 4d) (the photoresponsive characteristics of nanoporous MoS_2 under illumination of λ_{ex} = 638 nm are shown in Supplementary Fig. 8). The nanoporous MoS_2 photodetector exhibited a photoresponsivity of 622.2 A W⁻¹ (at P_{inc} = 0.8 mW cm⁻² and λ_{ex} = 405 nm), that is ~1240 times greater than the pristine MoS_2 phototransistor. To

confirm the reproducibility and reliability of the nanoporous MoS_2 phototransistors, we measured the photoresponsivity of five more multilayer nanoporous MoS_2 phototransistors with different channel areas. Supplementary Figure 9 shows average photoresponsivity and standard error of six nanoporous MoS_2 phototransistors, presenting consistent photoresponsivity with a very small standard error. Our result was compared with several papers that report the enhancement of photoresponsivity of the multilayer MoS_2 by applying various methods. Supplementary Figure 10 shows the relationship between photoresponsivity and P_{inc} extracted from various papers. The trend line (blue dotted line) of photoresponsivity of the nanoporous MoS_2 phototransistor is higher than most other devices except one having a heterostructure with direct bandgap monolayer MoS_2. The photodetection characteristics were also evaluated by specific detectivity ($D^* = R\sqrt{A/2qI_{dark}}$) and sensitivity ($S = I_{ph}/I_{dark}$), where A is the illuminated area and q is elementary charge. Significant increases in detectivity and sensitivity have been observed for the nanoporous MoS_2 phototransistor, as compared with the pristine MoS_2 counterpart (Fig. 4e, f). In addition, time-traced photoresponsive characteristic of the nanoporous MoS_2 phototransistor was measured under repetitive illumination with λ_{ex} of 405 nm and P_{inc} of 25 mW cm⁻² (Supplementary Fig. 11). Rising and decay time were approximately 1.01 s and 4.02 s, respectively.

To develop further insight into the nanoporous MoS_2 phototransistor exhibiting excellent optical properties, quantum transport simulations were performed considering the in-gap states that can trap electrons or holes (see Methods section for details of the simulation approach)[50]. As demonstrated by the PECCS measurements, the nanoporous MoS_2 contained multiple states within the bandgap (Fig. 3c). However, only certain states could be major contributors to the ultra-high photoresponsivity. To test this hypothesis, we simulated drain current (I_{DS}) vs gate voltage (V_{GS}) behaviors of the nanoporous MoS_2 phototransistor in the dark and under illumination (P_{inc} = 417 mW cm⁻² and λ_{ex} = 405 nm), assuming a single trap state (trap concentration, P_t = 5 10²⁵ m⁻³) near conduction band (E_C) and valence band (E_V) in Fig. 5a, b, respectively. A notable observation from the simulated I_{DS}–V_{GS} curves is that, with the in-gap state near E_V, a significant ΔV_{TH} can be achieved (Fig. 5b), while this phenomenon did not appear with the trap state near E_C (Fig. 5a). When V_{GS} is high, the trap state near E_C is fully filled with electrons both in the dark and under illumination, due to the large number of electron carriers in E_C. In contrast, while the trap state near E_V is fully occupied by electrons in the dark, it can be partially filled by holes under illumination due to the increased hole
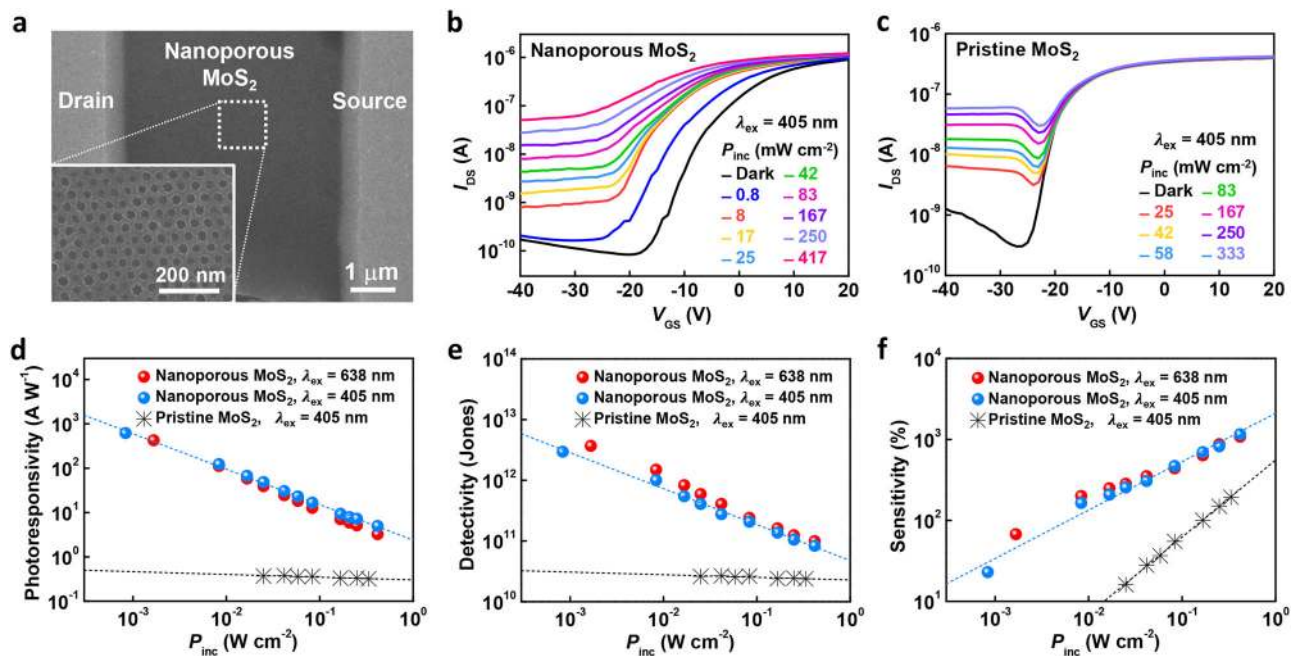
Fig. 4 Photoresponsive characteristics of the multilayer nanoporous MoS$_2$ TFTs. a SEM images of the nanoporous MoS$_2$ TFT. Transfer curves of **b** multilayer nanoporous MoS$_2$ and **c** pristine MoS$_2$ phototransistors in the dark and under illumination of λ_{ex} of 405 nm for various P_{inc}. **d** Calculated photoresponsivity, **e** specific detectivity, and **f** Sensitivity of the multilayer nanoporous and pristine MoS$_2$ phototransistors as a function of P_{inc}.
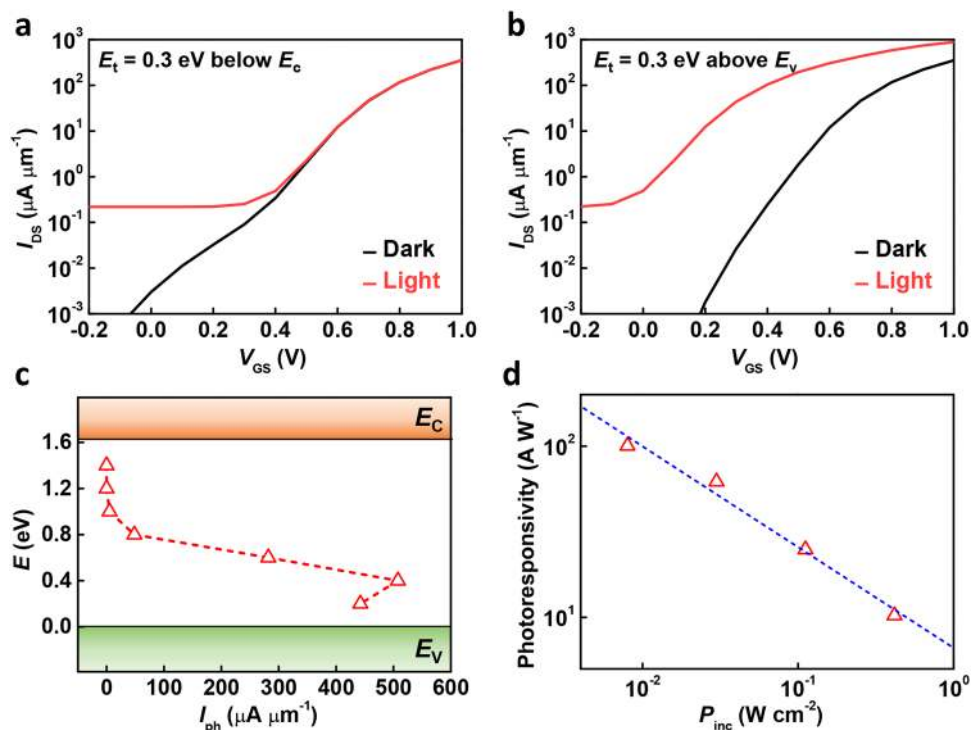

Fig. 5 Simulation of the photoresponsive behavior of the nanoporous MoS$_2$ phototransistor. Transfer characteristics of the nanoporous MoS$_2$ phototransistor assuming a single trap state (trap density of $P_t = 5 \times 10^{25}$ m^{-3}) near **a** E_C and **b** E_V in the dark and under illumination (λ_{ex} = 405 nm, P_{inc} = 417 mW cm^{-2}). **c** I_{ph} variation with a single trap state at different E_t within the bandgap (E_t from 0.2 eV to 1.4 eV above E_V) at V_{GS} = 1 V. **d** Photoresponsivity as a function of P_{inc} at λ_{ex} = 405 nm with trap states at four different energy levels (the dashed line is a guide to the eye). E_t = 0.3 and 0.4 eV above (below) E_V (E_C). The total trap density is the same as in Fig. 5a–c (i.e., 1.25×10^{25} m^{-3}).

concentration in the valence band with the generated excess holes, resulting in potential barrier lowering (i.e., the photogating effect). Our simulation results indicated that only the in-gap states near E_V can play an important role in the photogating effect, significantly increasing the electron injection from the source. It should be noted that the simulated I_{DS}–V_{GS} characteristics shown in Fig. 5b manifest the same trend as the measured I_{DS}–V_{GS} curves (Fig. 4b), which implies the presence of in-gap states near E_V in the nanoporous MoS_2 TFT.

To examine the impact of trap states at different energy levels (E_t), we have calculated I_{ph} by varying E_t from 0.2 eV to 1.4 eV above E_V in Fig. 5c, which reveals that I_{ph} can be significant only when the trap states are located near E_V (E_t–$E_V \leq 0.8$ eV). Finally, the photoresponsivity was plotted as a function of P_{inc} in Fig. 5d. To emulate the realistic material properties of the nanoporous MoS_2 including multiple trap states, we have included four trap states at $E_t = 0.3$ and 0.4 eV above E_V and below E_C with a trap concentration of 1.25×10^{25} m^{-3} each. The simulated photoresponsivity exhibits the same trend as the experimental results (Fig. 4d), indicating that our model could explain the underlying physics of the experimentally demonstrated nanoporous MoS_2 phototransistor.

Conclusion

Nano-scale patterning on multilayer MoS_2 was achieved by BCP lithography. A novel phototransistor based on the multilayer nanoporous MoS_2 channel exhibited significant enhancement in photoresponsivity, specific detectivity and photosensitivity, as compared with pristine multilayer MoS_2 phototransistors. A combination of Raman, XPS, and STEM-EDX measurements confirmed that the nanoporous structure, consisting of hexagonal arrays of hexagon holes, has abundant zigzag edges exposed with Mo- and S-termination. By means of PECCS experiment, it was shown that the nanoporous MoS_2 has high density of trap states into the bandgap region, and the device simulation revealed that the trap states existing near E_V are particularly crucial for the photogating effect and the overall optoelectronic performance of the nanoporous MoS_2 phototransistors. Hence, this work suggests using nano-patterning on multilayer MoS_2 for highly sensitive and responsive 2D material phototransistors.

Methods

Preparation of BCP nanotemplate. Sheets of multilayer MoS_2 were mechanically exfoliated from bulk, and then positioned on a Si/SiO$_2$ substrate. As a protective layer, SiO$_2$ with a thickness of 10 nm was deposited on the MoS_2 by e-beam evaporator. The entire substrate was then spin-coated with 1 wt% toluene solution of poly (styrene–r–methyl methacrylate) (Polymer source, $M_n = 8500$, $M_w/M_n =$ 1.45) (P(S-r-MMA)) RCP at 3000 rpm. To stabilize the thin film of the RCP, the sample was annealed at 250 °C under vacuum condition for 2 h, followed by washing with toluene. The substrate was then spin-coated with 1 wt% toluene solution of poly (styrene-b-methyl methacrylate) (Polymer source, PS = 55,000, PMMA = 22,000, $M_w/M_n = 1.09$) (P(S–b–MMA)) BCP at 3000 rpm, and then annealed at 230 °C for 2 h. UV irradiation (VL-6.LC, Vilber lourmat) was performed for 30 min to selectively remove the PMMA from the BCP upon immersion in acetic acid for 20 min.

Fabrication of nanoporous MoS_2 TFTs. The BCP nanotemplate was used as a mask to make the nanoporous MoS_2. The O$_2$ plasma RIE process (50 W, 10 s, 10 sccm) was performed to etch down to the RCP layer and increased the hole size of the nanotemplate. The SF$_6$ plasma RIE (200 W, 15 s, 10 sccm) was utilized to imprint the nanoholes onto the SiO$_2$ layer. MoS_2 was then etched using BCl$_3$ plasma RIE (100 W, 10 sccm) to produce the nanoporous MoS_2 by varying the etching time depending on the MoS_2 thickness. Then, the MoS_2 was immersed in diluted potassium ferricyanide solution for 30 s, resulting in a change in the nanohole shape from circular to hexagonal. Finally, the SiO$_2$ layer was removed by immersing the device in buffered oxide etchant.

To fabricate the nanoporous MoS_2 TFTs, the pattern of source and drain electrodes was prepared using photolithography and Ti (20 nm) and Au (100 nm) were deposited. After removing unnecessary portions, the TFTs were annealed under vacuum condition at 200 °C for 2 h to enhance the electrical behaviors.

Characterizations. Raman measurement was carried out using a Micro-Raman spectrometer system (ALPHA300, WITec) with a green excitation laser. A XPS system (K-Alpha, Thermo Fisher Scientific) with monochromated Al $K\alpha$ radiation was used to investigate the chemical states and stoichiometry of the MoS_2 samples. The surface morphologies and atomic structures of the nanoporous MoS_2 samples were observed on an aberration-corrected STEM (JEM-ARM200CF, JEOL) in ADF imaging mode at accelerating voltages of 80 and 200 kV, respectively. The angle range of the ADF detector and probe-forming convergence angle were 45–180 and 23 mrad, respectively. Wiener filtering technique inserted in commercial software was used to decrease random noise background in the obtained atomic-scale ADF-STEM images (HREM Filter Pro, HREM research). Elemental mapping of the nanoporous MoS_2 was carried out by EDX (JED-2300T, JEOL) with a dual-type Si drift detector operating in the same ADF-STEM imaging mode. Each detector had an effective X-ray sensing area of 100 mm^2, providing a total collection efficiency of ~10% of the total generated X-ray signals (4π sr). A semiconductor measurement system (4200-SCS, Keithley) equipped with a dark box was used for the electrical measurements. To measure the optoelectrical characteristics of the devices, laser radiation was perpendicularly incident on the MoS_2 channel area (MCLS1, Thorlabs) using single mode fiber optic patch cables (S405-HP for 405 nm and SM600 for 638 nm, Thorlabs).

Optoelectronic characterization. For PECCS measurements, the photo-excited transistor characterizations were carried out using an intense monochromatic light. The photon flux of almost 5×10^{14} cm^{-2} s^{-1} was estimated from the optical power density of ~0.1 mW cm^{-2}. The PECCS system consists of a grating monochromator providing a spectral wavelength range from 300 to 1400 nm, a Hg (Xe) light source of 500 W, and an optical fiber that delivers light to the reactive MoS_2 surface of the devices. Electrical measurements were performed by electrical analyzer unit (4155C, Agilent Technologies). Photoluminescence measurements were performed by a spectrometer system (ALPHA300, WITec) with a 532 nm excitation laser.

Device simulation. Carrier transport through the nanoporous MoS_2 phototransistor was simulated using the non-equilibrium Green's function (NEGF) formalism within an effective mass approximation ($m^* = 0.45 \ m_0$, where m_0 is the free electron mass). For the nominal device, a 50-nm-long, 6.2-Å-thick MoS_2 channel and a 2.5-nm-thick SiO$_2$ gate dielectric were used in a bottom-gate Schottky barrier (SB) field-effect transistor (FET) structure with an SB height of 0.1 eV. A power supply voltage of $V_{DD} = 0.5$ V was applied. Here, we used smaller device dimensions to save simulation time; however, this will not affect the key underlying physics, and the conclusion from the simulation study will remain the same. The transport equation was iteratively solved with Poisson's equation until a self-consistent solution was achieved. Here, we first performed a ballistic transport simulation assuming ideal MoS_2 to identify the underlying physics of the photogating effect (Fig. 5a–c), and then the current degradation due to scattering in the actual nanoporous structure was taken into account by calibrating the simulation results against the experiments (Fig. 5d) using a fitting parameter (degradation factor of 8×10^{-6}).

Trap model. A modified Hornbeck–Haynes model of $\triangle\sigma = q\mu_n \triangle n_{PC} + q\mu_p \triangle p_{PC}$ was used to calculate the increase in conductivity regarding to illumination (photoconductive (PC) effect), where μ_n and μ_p are the mobilities of electrons and holes, and $\triangle n_{PC}$ and $\triangle p_{PC}$ are electron and hole excess densities in the conduction and the valence band, respectively. Measured carrier mobility of 2.68 cm^2 V^{-1} s^{-1} was used for both μ_n and μ_p. Considering charge neutrality, $\triangle n_{PC} = g\tau_{r,PC}$ and $\triangle p_{PC} = \triangle n_{PC} + n_{t,PC}$ were used with the trap state near E_C, while $\triangle p_{PC} = g\tau_{r,PC}$ and $\triangle n_{PC} = \triangle p_{PC} + p_{t,PC}$ with the trap state near E_V, assuming that the fermi level is located at mid-gap[51]. $n_{t,PC}$ and $p_{t,PC}$ are the trapped electron and hole densities, which can be calculated as $n_{t,PC} = \frac{P_t dg\tau_{r,PC}}{g\tau_{r,PC} + P_t d\tau_{t,n}/\tau_{g,n}}$ and $p_{t,PC} = \frac{P_t dg\tau_{r,PC}}{g\tau_{r,PC} + P_t d\tau_{t,p}/\tau_{g,p}}$, where P_t is the total trap concentration[51]. $g(= \eta P_{abs}/h\nu)$ is the generation rate of excess carriers, d is the thickness of the nanoporous MoS_2, and $\tau_{r,PC}$ is the carrier recombination lifetime for the photoconductive effect. η and $h\nu$ are internal quantum efficiency and single photon energy, respectively. The value of η was assumed to be 0.5 for λ_{ex} of 405 nm. The absorbed power density (P_{abs}) is calculated by $P_{inc}\left(1 - \frac{e^{-a^\perp d} + e^{-a^\parallel d}}{2}\right)$, where $a^\perp$ and $a^\parallel$ are the absorption coefficients in the vertical ($a^\perp = 18.9 \times 10^4$ cm^{-1} at $\lambda_{ex} = 405$ nm)[52] and lateral ($a^\parallel = 102.5 \times 10^4$ cm^{-1} at $\lambda_{ex} = 405$ nm)[53] directions, respectively. $\tau_{t,n/p}$ and $\tau_{g,n/p}$ are the trapping and detrapping times of electrons/holes, respectively, and the $\frac{\tau_{t,n}}{\tau_{g,n}}$ and $\frac{\tau_{t,p}}{\tau_{g,p}}$ ratios can be obtained by $1/\left(\frac{P_t}{N_C}\exp\frac{\triangle E_{t,C}}{kT}\right)$ and $1/\left(\frac{P_t}{N_V}\exp\frac{\triangle E_{t,V}}{kT}\right)$[51], where N_C and N_V are effective density of states at E_C and E_V, respectively. $\triangle E_{t,C}$ and $\triangle E_{t,V}$ are defined as E_C–E_t and E_t–E_V, respectively. The recombination lifetime ($\tau_{r,PC} = 100$ ps) was adopted from a previous report[54]. Finally, photoconductive current ($I_{ph,PC}$) was obtained by $I_{ph,PC} = \frac{1}{L}V_{DS}\triangle\sigma$. The photogating (PG) effect due to barrier lowering can be simulated by considering trapped holes (i.e., total trap concentration – electrons in the trap state) as $p_{t,PG} = P_t(1 - f)$, where f is the probability of electron occupation at a given trap state, which can be calculated by $f = \frac{v_{th}\sigma_n n_C + e_p}{v_{th}\sigma_n n_C + e_n + v_{th}\sigma_p p_V + e_p}$[54]. n_C and p_V are concentration of electrons in the conduction band and concentration of holes in the valence band, respectively, and v_{th} is thermal velocity. e_n and e_p are the probabilities of

electron and hole emission from the trap state, respectively, determined by $e_n = v_{th}\,\sigma_n n_0 \exp\frac{E_t - E_{F0}}{kT}$ and $e_p = v_{th}\,\sigma_p p_0 \exp\frac{E_{F0} - E_t}{kT}$, where σ_n and σ_p are capture cross-sections for electrons and holes, respectively[54]. n_0 and p_0 are the concentration of free electrons in the conduction band and the concentration of free holes in the valence band, respectively, under equilibrium, which are defined as $n_0 = N_C \ln(1 + \exp\{(E_{F0} - E_C)/kT\})$ and $p_0 = N_V \ln(1 + \exp\{(E_V - E_{F0})/kT\})$, where E_{F0} is the fermi level under thermal equilibrium assumed to be at mid-gap in this study. For n-type transistors, the electron concentration (n_C) is obtained by $n_C = n_{inj} + \triangle n_{ph}$, where n_{inj} is the injected electron concentration obtained from the NEGF simulation. Under illumination, the excess electron concentration becomes a non-zero value, which can be modeled as $\triangle n_{ph} = g\tau_{r,PG}/d$, where the recombination lifetime for the pho-togating effect ($\tau_{r,PG}$) was assumed to be 1 µs. The hole concentration (p_V) is mainly determined by the excess hole concentration ($\triangle p_{ph}$), which is the same as $\triangle n_{ph}$. For a given trap state, f is a strong function of $\frac{\sigma_n}{\sigma_p}$, which was assumed to be a logistic function of energy in a logarithmic scale with maximum and minimum values of 10^3 and 10^{-3} at E_C and E_V edges, respectively. Since the trap sites are negatively charged in the presence of electrons, the concentration of trapped electrons ($n_{t,PG} = P_t - p_{t,PG}$) was considered in Poisson's equation as follows:
$$\nabla^2 V = -\frac{q}{\varepsilon}\{N_D - N_A + p_V - (n_C + n_{t,PG})\}.$$

Data availability

The data presented in this study are available from the corresponding author upon reasonable request.

References

1. Fossum, E. R. CMOS image sensors: electronic camera-on-a-chip. *IEEE Trans. Electron Devices* **44**, 1689–1698 (1997).
2. Ohta, J. *Smart CMOS Image Sensors And Applications* (CRC press, 2007).
3. Ahn, S. E. et al. Metal oxide thin film phototransistor for remote touch interactive displays. *Adv. Mater.* **24**, 2631–2636 (2012).
4. Liu, X. et al. Scalable integration of indium zinc oxide/photosensitive-nanowire composite thin-film transistors for transparent multicolor photodetectors array. *Adv. Mater.* **26**, 2919–2924 (2014).
5. Chu, Y. et al. Photosensitive and flexible organic field-effect transistors based on interface trapping effect and their application in 2D imaging array. *Adv. Sci.* **3**, 1500435 (2016).
6. Jeon, S. et al. Gated three-terminal device architecture to eliminate persistent photoconductivity in oxide semiconductor photosensor arrays. *Nat. Mater.* **11**, 301–305 (2012).
7. Bertolazzi, S., Brivio, J. & Kis, A. Stretching and breaking of ultrathin MoS$_2$. *ACS Nano* **5**, 9703–9709 (2011).
8. Kwon, J. et al. Giant photoamplification in indirect-bandgap multilayer MoS$_2$ phototransistors with local bottom-gate structures. *Adv. Mater.* **27**, 2224–2230 (2015).
9. Jariwala, D. et al. Emerging device applications for semiconducting two-dimensional transition metal dichalcogenides. *ACS Nano* **8**, 1102–1120 (2014).
10. Buscema, M. et al. Photocurrent generation with two-dimensional van der Waals semiconductors. *Chem. Soc. Rev.* **44**, 3691–3718 (2015).
11. Schmidt, H., Giustiniano, F. & Eda, G. Electronic transport properties of transition metal dichalcogenide field-effect devices: surface and interface effects. *Chem. Soc. Rev.* **44**, 7715–7736 (2015).
12. Li, S. L., Tsukagoshi, K., Orgiu, E. & Samori, P. Charge transport and mobility engineering in two-dimensional transition metal chalcogenide semiconductors. *Chem. Soc. Rev.* **45**, 118–151 (2016).
13. Wang, Q. H. et al. Electronics and optoelectronics of two-dimensional transition metal dichalcogenides. *Nat. Nanotechnol.* **7**, 699–712 (2012).
14. Chhowalla, M. et al. The chemistry of two-dimensional layered transition metal dichalcogenide nanosheets. *Nat. Chem.* **5**, 263–275 (2013).
15. Zhang, Y. et al. Direct observation of the transition from indirect to direct bandgap in atomically thin epitaxial MoSe$_2$. *Nat. Nanotechnol.* **9**, 111–115 (2014).
16. Mak, K. F. et al. Atomically thin MoS$_2$: a new direct-gap semiconductor. *Phys. Rev. Lett.* **105**, 136805 (2010).
17. Tongay, S. et al. Thermally driven crossover from indirect toward direct bandgap in 2D semiconductors: MoSe$_2$ versus MoS$_2$. *Nano Lett.* **12**, 5576–5580 (2012).
18. Choi, W. et al. High-detectivity multilayer MoS$_2$ phototransistors with spectral response from ultraviolet to infrared. *Adv. Mater.* **24**, 5832–5836 (2012).
19. Kim, S. et al. High-mobility and low-power thin-film transistors based on multilayer MoS$_2$ crystals. *Nat. Commun.* **3**, 1011 (2012).
20. Yun, T. et al. 2D Metal chalcogenide nanopatterns by block copolymer lithography. *Adv. Funct. Mater.* **28**, 1804508 (2018).
21. Xue, H. et al. High photoresponsivity and broadband photodetection with a band-engineered WSe$_2$/SnSe$_2$ heterostructure. *Nanoscale* **11**, 3240–3247 (2019).
22. Nazir, G. et al. Enhanced photoresponse of ZnO quantum dot-decorated MoS$_2$ thin films. *RSC Adv.* **7**, 16890–16900 (2017).
23. Chen, C. Y. et al. Highly responsive MoS$_2$ photodetectors enhanced by graphene quantum dots. *Sci. Rep.* **5**, 11830 (2015).
24. Qiao, S. et al. A vertically layered MoS$_2$/Si heterojunction for an ultrahigh and ultrafast photoresponse photodetector. *J. Mater. Chem. C* **6**, 3233–3239 (2018).
25. Zeng, Z. Y. et al. Fabrication of graphene nanomesh by using an anodic aluminum oxide membrane as a template. *Adv. Mater.* **24**, 4138–4142 (2012).
26. Bai, J. W. et al. Graphene nanomesh. *Nat. Nanotechnol.* **5**, 190–194 (2010).
27. Liang, X. G. et al. Formation of bandgap and subbands in graphene nanomeshes with sub-10 nm ribbon width fabricated via nanoimprint lithography. *Nano Lett.* **10**, 2454–2460 (2010).
28. Kim, M. et al. Fabrication and characterization of large-area, semiconducting nanoperforated graphene materials. *Nano Lett.* **10**, 1125–1131 (2010).
29. Kim, T. et al. Structural defects in a nanomesh of bulk MoS$_2$ using an anodic aluminum oxide template for photoluminescence efficiency enhancement. *Sci. Rep.* **8**, 6648 (2018).
30. Krishnamoorthy, S., Hinderling, C. & Heinzelmann, H. Nanoscale patterning with block copolymers. *Mater. Today* **9**, 40–47 (2006).
31. Bang, J. et al. Block copolymer nanolithography: translation of molecular level control to nanoscale patterns. *Adv. Mater.* **21**, 4769–4792 (2009).
32. Kim, H. C., Park, S. M. & Hinsberg, W. D. Block copolymer based nanostructures: materials, processes, and applications to electronics. *Chem. Rev.* **110**, 146–177 (2010).
33. Yin, Z. Y. et al. Single-layer MoS$_2$ phototransistors. *ACS Nano* **6**, 74–80 (2012).
34. Lopez-Sanchez, O. et al. Ultrasensitive photodetectors based on monolayer MoS$_2$. *Nat. Nanotechnol.* **8**, 497–501 (2013).
35. Zhang, W. J. et al. High-gain phototransistors based on a CVD MoS$_2$ monolayer. *Adv. Mater.* **25**, 3456–3461 (2013).
36. Im, S., Chang, Y.-G. & Kim, J. H. *Photo-Excited Charge Collection Spectroscopy: Probing The Traps In Field-effect Transistors* (Springer Science & Business Media, 2014).
37. Ferrarese Lupi, F. et al. High aspect ratio PS-b-PMMA block copolymer masks for lithographic applications. *ACS Appl. Mater. Interfaces* **6**, 21389–21396 (2014).
38. Li, H. et al. From bulk to monolayer MoS$_2$: evolution of raman scattering. *Adv. Funct. Mater.* **22**, 1385–1390 (2012).
39. Verble, J. L. & Wieting, T. J. Lattice mode degeneracy in MoS$_2$ and other layer compounds. *Phys. Rev. Lett.* **25**, 362–365 (1970).
40. Kong, D. S. et al. Synthesis of MoS$_2$ and MoSe$_2$ films with vertically aligned layers. *Nano Lett.* **13**, 1341–1347 (2013).
41. Kim, I. S. et al. Influence of stoichiometry on the optical and electrical properties of chemical vapor deposition derived MoS$_2$. *ACS Nano* **8**, 10551–10558 (2014).
42. Lin, H. B. et al. Electrocatalysis of polysulfide conversion by sulfur-deficient MoS$_2$ nanoflakes for lithium-sulfur batteries. *Energy Environ. Sci.* **10**, 1476–1486 (2017).
43. Sim, D. M. et al. Controlled doping of vacancy-containing few-layer MoS$_2$ via highly stable thiol-based molecular chemisorption. *ACS Nano* **9**, 12115–12123 (2015).
44. Kondekar, N. P., Boebinger, M. G., Woods, E. V. & McDowell, M. T. In situ XPS investigation of transformations at crystallographically oriented MoS$_2$ interfaces. *ACS Appl. Mater. Interfaces* **9**, 32394–32404 (2017).
45. Tinoco, M. et al. Strain-dependent edge structures in MoS$_2$ layers. *Nano Lett.* **17**, 7021–7026 (2017).
46. Yang, S. Q. et al. First-principles study of zigzag MoS$_2$ nanoribbon as a promising cathode material for rechargeable Mg batteries. *J. Phys. Chem. C* **116**, 1307–1312 (2012).
47. Xiao, S. L., Yu, W. Z. & Gao, S. P. Edge preference and band gap characters of MoS$_2$ and WS$_2$ nanoribbons. *Surf. Sci.* **653**, 107–112 (2016).
48. Li, Y. F., Zhou, Z., Zhang, S. B. & Chen, Z. F. MoS$_2$ nanoribbons: high stability and unusual electronic and magnetic properties. *J. Am. Chem. Soc.* **130**, 16739–16744 (2008).
49. Kim, S. et al. Interstitial Mo-assisted photovoltaic effect in multilayer MoSe$_2$ phototransistors. *Adv. Mater.* **30**, 1705542 (2018).
50. Han, G., Kaniselvan, M. & Yoon, Y. Photoresponse of MoSe$_2$ transistors: A fully numerical quantum transport simulation study. *ACS Appl. Electron. Mater.* **2**, 3765–3772 (2020).
51. Furchi, M. M., Polyushkin, D. K., Pospischil, A. & Mueller, T. Mechanisms of photoconductivity in atomically thin MoS$_2$. *Nano Lett.* **14**, 6165–6170 (2014).
52. Perdew, J. P., Burke, K. & Ernzerhof, M. Generalized gradient approximation made simple. *Phys. Rev. Lett.* **77**, 3865–3868 (1996).
53. Ahuja, U. et al. Optical response of mixed molybdenum dichalcogenides for solar cell applications using the modified Becke-Johnson potential. *Z. Naturforsch. A* **71**, 213–223 (2016).

54. Simmons, J. G. & Taylor, G. W. Nonequilibrium steady-state statistics and associated effects for insulators and semiconductors containing an arbitrary distribution of traps. *Phys. Rev. B* **4**, 502–511 (1971).

Author contributions

S.K. and Y.Y. conceived the project. H.P., Y.J.K. and S.K. fabricated the nanoporous MoS_2 structure using BCP lithography and measured the electrical properties of the nanoporous MoS_2 phototransistors. J.L. and H.P. performed PECCS measurements on nanoporous MoS_2 phototransistors and analyzed optoelectronic characterization of MoS_2 nanosheet. G.H., A.A.M., J.L. and Y.Y. performed theoretical simulations of the nanoporous MoS_2 phototransistor behavior. Y.-H.K. and Y.-M.K. contributed to structural and chemical characterizations of the nanoporous MoS_2 using STEM. All authors wrote and contributed to the manuscript.

Competing interests

S.K. is an editorial board member for Communications Materials and was not involved in the editorial review, or the decision to publish, this article. All authors declare that there are no competing interests.

Additional information

Supplementary information The online version contains supplementary material available at https://doi.org/10.1038/s43246-021-00197-0.

Correspondence and requests for materials should be addressed to Young-Min Kim, Young Jun Kim, Youngki Yoon or Sunkook Kim.

Peer review information *Communications Materials* thanks the anonymous reviewers for their contribution to the peer review of this work. Primary Handling Editors: Aldo Isidori.

Reprints and permission information is available at http://www.nature.com/reprints

Publisher's note Springer Nature remains neutral with regard to jurisdictional claims in published maps and institutional affiliations.